



Article

Influence of Wurtzite ZnO Morphology on Piezophototronic Effect in Photocatalysis

Xiaowen Su ¹, Xiaolei Zhao ¹, Chao Cui ¹, Ning Xi ¹, Xiao Li Zhang ², Hong Liu ¹, Xiaowen Yu ^{1,*} 
and Yuanhua Sang ^{1,*} ¹ State Key Laboratory of Crystal Materials, Shandong University, Jinan 250100, China² State Centre for International Cooperation on Designer Low-Carbon & Environmental Materials, School of Materials Science and Engineering, Zhengzhou University, Zhengzhou 450001, China

* Correspondence: xiaowen.yu@sdu.edu.cn (X.Y.); sangyh@sdu.edu.cn (Y.S.)

Abstract: A piezoelectric field promotes the photocatalytic activity of a photocatalyst by helping separating photo-generated charge carriers. Wurtzite phase ZnO is a typical photocatalyst with a piezoelectric property, thus self-assisted photocatalysis with ZnO based on the piezophototronic effect can be achieved. ZnO nanorods or nanowires with a clear c-axis have been well studied, while other morphologies have not been fully discussed. In this work, we prepared wurtzite phase ZnO with four different morphologies. By comparing their photocatalytic activity for degradation of Rhodamine B under the same mechanical energy source provided by ultrasound, the effect of morphology and exposed facets on photo-induced charge separation were highlighted. The ZnO nanowire photocatalyst delivered an impressive improvement in photocatalytic efficiency when ultrasound driven, suggesting that the morphology-related piezophototronic effect had a positive effect on separation of photo-generated charge carriers, and more exposed active facets benefitted the utilization of charge carriers.

Keywords: ZnO; photocatalysis; morphology; piezophototronic effect

Citation: Su, X.; Zhao, X.; Cui, C.; Xi, N.; Zhang, X.L.; Liu, H.; Yu, X.; Sang, Y. Influence of Wurtzite ZnO

Morphology on Piezophototronic Effect in Photocatalysis. *Catalysts* **2022**, *12*, 946. <https://doi.org/10.3390/catal12090946>

Academic Editor: Ewa Kowalska

Received: 13 July 2022

Accepted: 23 August 2022

Published: 25 August 2022

Publisher's Note: MDPI stays neutral with regard to jurisdictional claims in published maps and institutional affiliations.



Copyright: © 2022 by the authors. Licensee MDPI, Basel, Switzerland. This article is an open access article distributed under the terms and conditions of the Creative Commons Attribution (CC BY) license (<https://creativecommons.org/licenses/by/4.0/>).

1. Introduction

Water pollution has become a hot issue in recent years. Toxic compounds in water can cause an ecological crisis and negative effects on human health [1,2]. Organic pollutant, such as dyes, antibiotics, and surfactants, are typical pollutants in effluent wastewater, which mainly comes from paper, textile, and apparel industries [3]. Dyes usually have complex chemical structures; they are stable to light and oxidation and are very difficult to biodegrade; they are toxic to aquatic life and cause severe health hazards to human beings. Thus, it is urgent to treat dyes before discharging them into water, or to remove dyes in wastewater [4]. A variety of emerging technologies have been developed, such as adsorption, precipitation, membrane separation, and electro dialysis [5–9]. Though these conventional technologies are promising in practical applications, they suffer from low efficiency, high cost, and secondary pollution [10]. In contrast, photocatalysis, as a new environmentally friendly technology, has drawn a great attention due to its low cost and green process [11]. So far, photocatalysis technology has been applied in many fields, such as wastewater treatment [12,13], photocatalytic hydrogen generation [14,15], and photocatalytic CO₂ reduction [16,17]. In a typical photocatalytic process, the selectivity for a photocatalyst is first taken into account. Many photocatalysts, such as TiO₂ [18,19], CdS [20–22], BiVO₄ [23,24] and Ag₂O [25,26], have been used for wastewater treatment. Among them, ZnO is a typical semiconductor photocatalyst with a wide bandgap of about 3.2 eV. It has advantages of being nontoxic, low-cost, and has easy-synthesis; however, it often suffers from a high recombination rate of photo-induced charge carriers in photocatalysis, which decreases the photocatalytic efficiency and limits its practical application [27–29]. Thus, searching effective techniques to avoid or alleviate the recombination

of photo-induced charges in the ZnO photocatalyst has become a big challenge. Substantial efforts have been devoted to this aspect, such as doping [30,31], designing Z-scheme heterostructure photocatalysts [32–34], and so on. The piezophototronic effect of a metal-ZnO system was discovered in 2010, and revealed that the piezoelectric effect could significantly enhance the Schottky barrier height, while photon excitation lowered the Schottky barrier due to increased local carrier density, resulting in tuning piezoelectric polarization charges, and thereby affecting carrier separation, recombination, and transport. [35]. As one of the piezoelectric materials with photocatalytic activity, ZnO can generate a polarization electric field upon piezo-excitation, which is beneficial for separating photo-generated carriers in photocatalytic processes [36,37]. Furthermore, some works have introduced ultrasonic wave as an irradiation energy source to vibrate the photocatalysts and enhance their photocatalytic efficiency. For example, Bai et al. reported that ZnO nanorods created a piezoelectric field under water flow, and the generated piezoelectric field enhanced the photocatalytic activity [38]. Wu et al. designed a water flow-driven piezophotocatalytic flexible film by bi-piezoelectric integration of ZnO nanorods and polyvinylidene fluoride (PVDF), which presented a significant improvement in photocatalytic activity related to piezoelectric property [39]. So far, most cases have focused on ZnO nanowires or nanorods with wurtzite structure. This is because wurtzite ZnO nanowires have a clear c-axis, which can deform under mechanical energy provided by tide or sonic effects and result in producing piezoelectric field on the surface [40,41]. However, the influences of morphology on the piezoelectric field of wurtzite ZnO has rarely been discussed.

In this current work, we synthesized four wurtzite ZnO samples with different morphologies by varying the type and concentration of precipitants. Rhodamine B (RhB) was used as a model dye to evaluate photocatalytic efficiency and enhancement brought about by an ultrasound-produced piezoelectric field. A majority of prepared ZnO samples showed improvement in photocatalytic efficiency upon ultrasonic vibration, implying that the piezoelectric field induced by ultrasound produced a positive effect on suppressing the recombination of photo-generated charge carriers. In particular, the impressively enhanced photocatalytic efficiency of the ZnO nanowire photocatalyst under ultrasound indicated a morphology influence on the piezoelectric field.

2. Results and Discussion

As shown in Figure 1a, the XRD patterns of samples with different morphologies all fit well with the hexagonal wurtzite ZnO (JCPDS card no. 36-1451). The diffraction peaks at 31.8° , 34.4° , 36.2° , 47.5° and 56.6° are indexed to the (100), (002), (101), (102), and (110) crystal planes of ZnO, respectively [42]. No extra peaks were detected in the XRD patterns, implying high purity of these ZnO samples. The XRD patterns were all unified by the intensity of the (101) crystal plane for each sample. The diffraction intensities of other crystal planes were similar in four samples. The distinct and sharp peaks in the XRD patterns suggested that the as-obtained ZnO samples had good crystallinity. The relatively broaden peaks for the ZnO nanosphere sample indicated a relatively poor crystallinity, which was attributed to the small crystalline size ~ 10 nm analyzed according to the Scherrer Formula [43]. As shown in the Raman spectra (Figure 1b), there are two distinct peaks at 334 and 436 cm^{-1} , which can be assigned to $E_2^{(\text{low})}$ (E_{2l}) and $E_2^{(\text{high})}$ (E_{2h}) modes of ZnO, respectively. The peak at 580 cm^{-1} is ascribed as E_1 (LO) mode of ZnO [44]. No detectable difference was identified in the Raman spectra, which further reveals similar crystal structures of the as-obtained four ZnO samples.

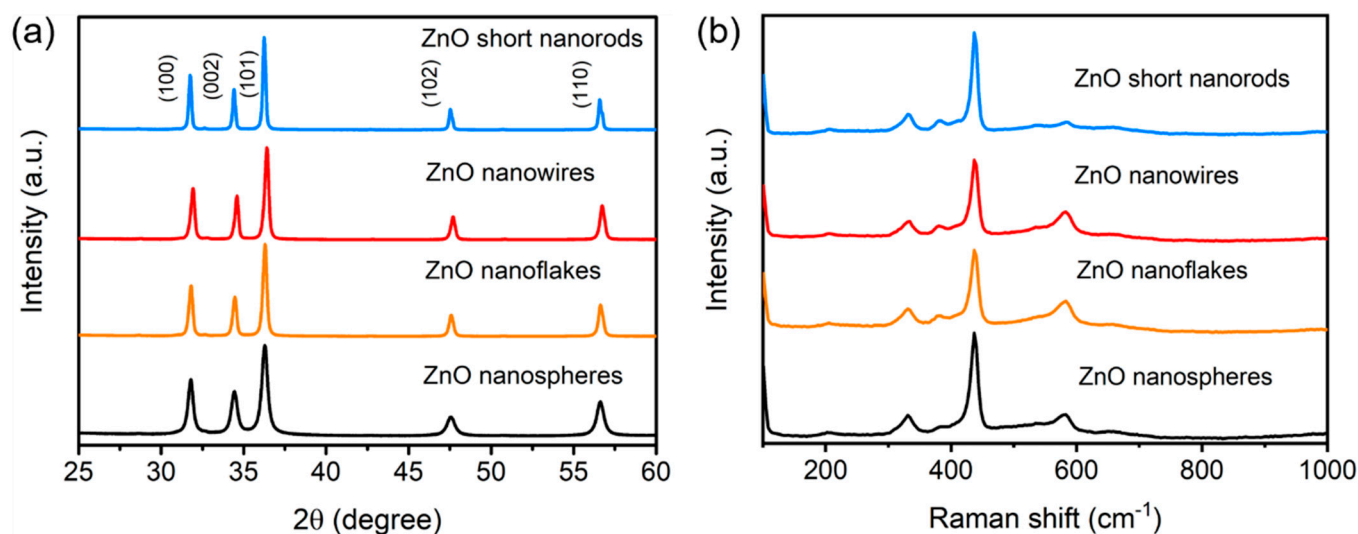


Figure 1. (a) XRD patterns of ZnO samples with four different morphologies. (b) Raman spectra of ZnO samples with four different morphologies.

Figure 2 displays SEM and TEM images as well as morphology schematics of the ZnO samples. Due to different synthesis methods, the four samples had different morphologies. As shown in Figure 2a–d, when using NaOH as a precipitant with a low concentration (0.1 M) during preparation, ZnO grew into short nanorods with a regular hexagon section (see Figure 2b). The corresponding HRTEM image shows a distinct lattice fringe with a d spacing of 0.247 nm, ascribed to the (101) plane of ZnO (Figure 2c). When increasing the concentration of NaOH to 1.0 M, the morphology of ZnO changed to nanowires with lengths of about 3–4 μm (see Figure 2e,f). The HRTEM image in Figure 2g shows a well-defined lattice fringe with a d spacing of 0.247 nm, which can be indexed to (101) plane of ZnO. The exposure of the (101) plane on both ZnO nanorod and nanowire samples implies that they follow the same crystal growth direction. When using other precipitants, the ZnO morphologies were diverse. For example, when urea worked as a precipitant, ZnO was assembled as cabbage-like nanoclusters composed of nanoflakes (see Figure 2i–l). An individual nanoflake exhibited lattice fringes with d spacings of 0.247 and 0.281 nm, which correspond to (101) and (110) planes of ZnO, respectively (see Figure 2k). The formation and assembling of ZnO nanoparticles with urea as the precipitant was attributed to burst nucleation during the temperature controlled hydrolyzation of urea [45]. When TEOA was added as a surface modification agent, ZnO was assembled as nanospheres with diameters of 400–500 nm consisting of small nanoparticles (see Figure 2m–p). The nanoparticles had sizes of 20–30 nm as discussed in our previous work [46]. The nanoparticle displayed a lattice fringe with a d spacing of 0.191 nm, which can be ascribed to the (102) plane of ZnO.

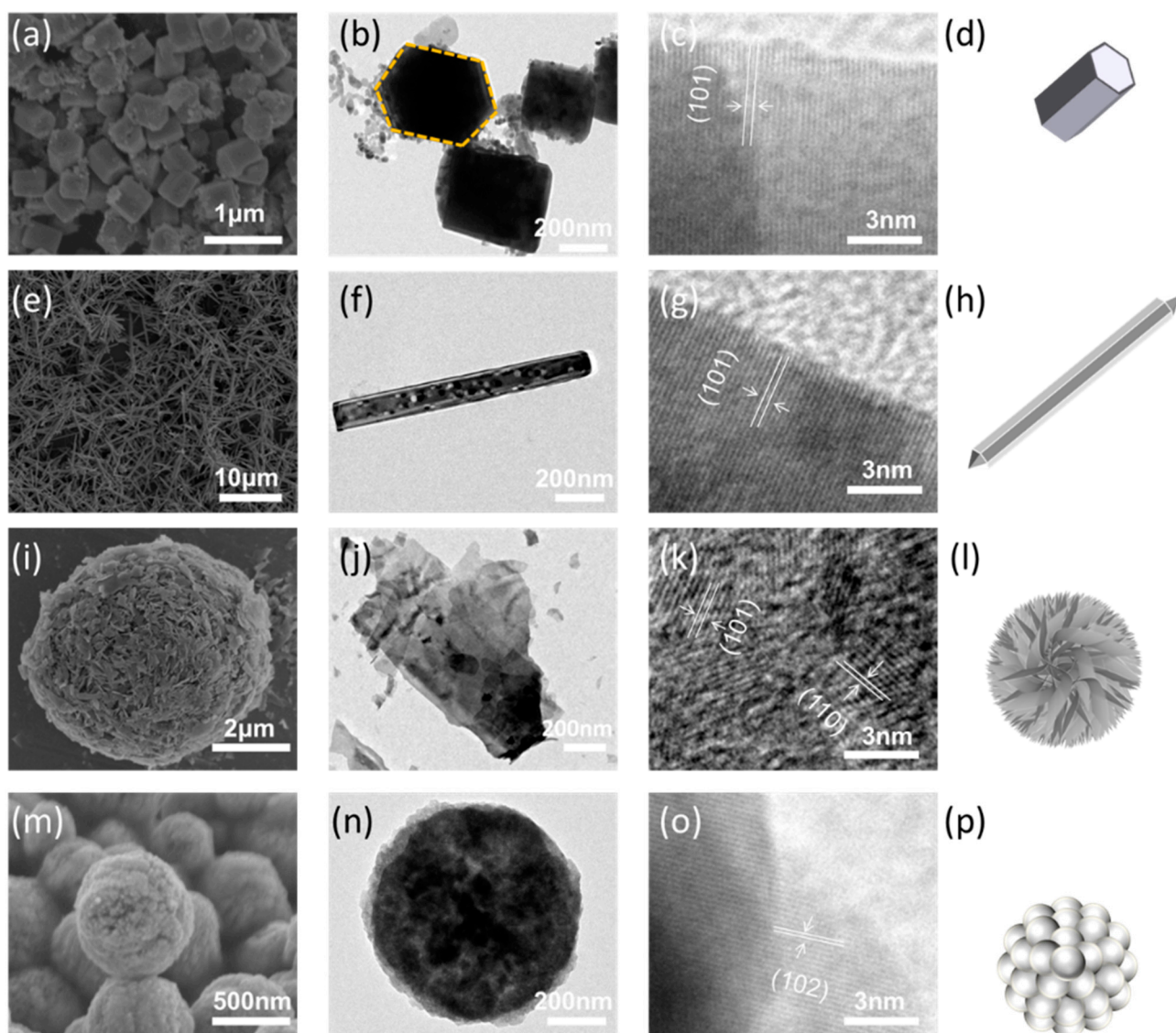


Figure 2. (a) SEM, (b) TEM, (c) HRTEM images, and (d) morphology schematic of ZnO short nanorods. (e) SEM, (f) TEM, (g) HRTEM images, and (h) morphology schematic of ZnO nanowires. (i) SEM, (j) TEM, (k) HRTEM images, and (l) morphology schematic of ZnO nanoflakes. (m) SEM, (n) TEM, (o) HRTEM images, and (p) morphology schematic of ZnO nanospheres.

XPS spectra were analyzed to reveal the chemical binding states of elements in the ZnO samples (Figure 3). For the ZnO short nanorod sample, Zn 2p XPS spectra displayed two distinct peaks located at 1021.7 and 1044.75 eV, corresponding to the $2p_{3/2}$ and $2p_{1/2}$ doublets of Zn^{2+} (see Figure 3a) [47]. O 1s XPS spectra could be deconvoluted into two peaks at 530.37 and 531.72 eV, which can be indexed to Zn-O and hydroxyl oxygen on the sample surface [48], respectively (see Figure 3b). The other ZnO samples with different morphologies (nanowires, nanoflakes, and nanospheres) showed similar Zn 2p and O 1s XPS spectra to the ZnO short nanorods (see Figure 3c–h), indicating that these four ZnO samples have similar chemical states of Zn and O.

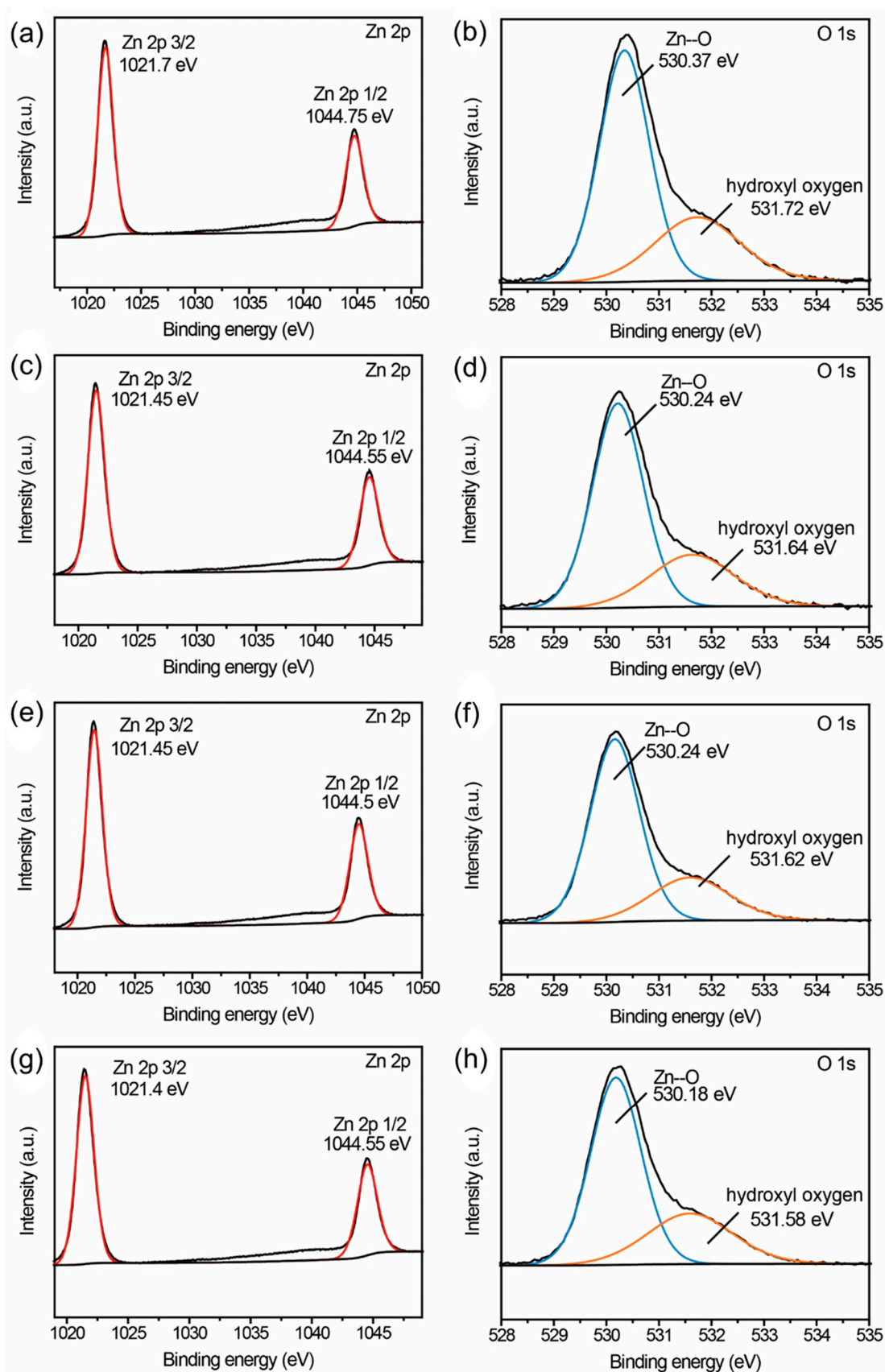


Figure 3. XPS spectra of (a) Zn 2p and (b) O 1s of ZnO short nanorods, (c) Zn 2p and (d) O 1s of ZnO nanowires, (e) Zn 2p and (f) O 1s of ZnO nanoflakes, (g) Zn 2p and (h) O 1s of ZnO nanospheres.

The optical properties of four ZnO samples were analyzed by UV-Vis spectroscopy (see Figure 4a). All samples showed similar absorption spectra with significant absorption intensity below 400 nm wavelength, indicating that these samples mainly absorb UV lights. The band gaps of the ZnO samples were calculated by following the equation [49]:

$$(\alpha h\nu)^2 = C (h\nu - E_g) \quad (1)$$

where, α , h , ν , C , and E_g refer to absorption coefficient, Planck constant, frequency of photon, absorption constant, and band gap energy, respectively. The intersection in the abscissa axis for the linear fit in the graph between $(\alpha h\nu)^2$ and incident energy of photon ($h\nu$) gave the E_g value [50]. The ZnO samples with different morphologies showed slightly different band gap values of 3.18, 3.04, 3.15, and 3.05 eV for the ZnO nanorods, nanowires, nanoflakes, and nanospheres, respectively. The difference may arise from different defect states, especially the surface defects in the nanostructures with different morphologies. PL spectra were recorded to evaluate the recombination property of photo-induced charge carriers in different samples (see Figure 4f). At room temperature, four ZnO samples all showed broad bands between 400 to 700 nm. The broad emission characteristic was attributed to the oxygen vacancies [51]. It was noted that the shoulder peak at 650 nm of ZnO nanorods was due to band transition from Zn_i to O_i level [52]. Notably, the short nanorod ZnO sample performed the highest PL intensity, indicating the heaviest recombination of photo-generated electron-hole pairs. Other samples displayed decreased PL intensities, suggesting the suppressed charge recombination.

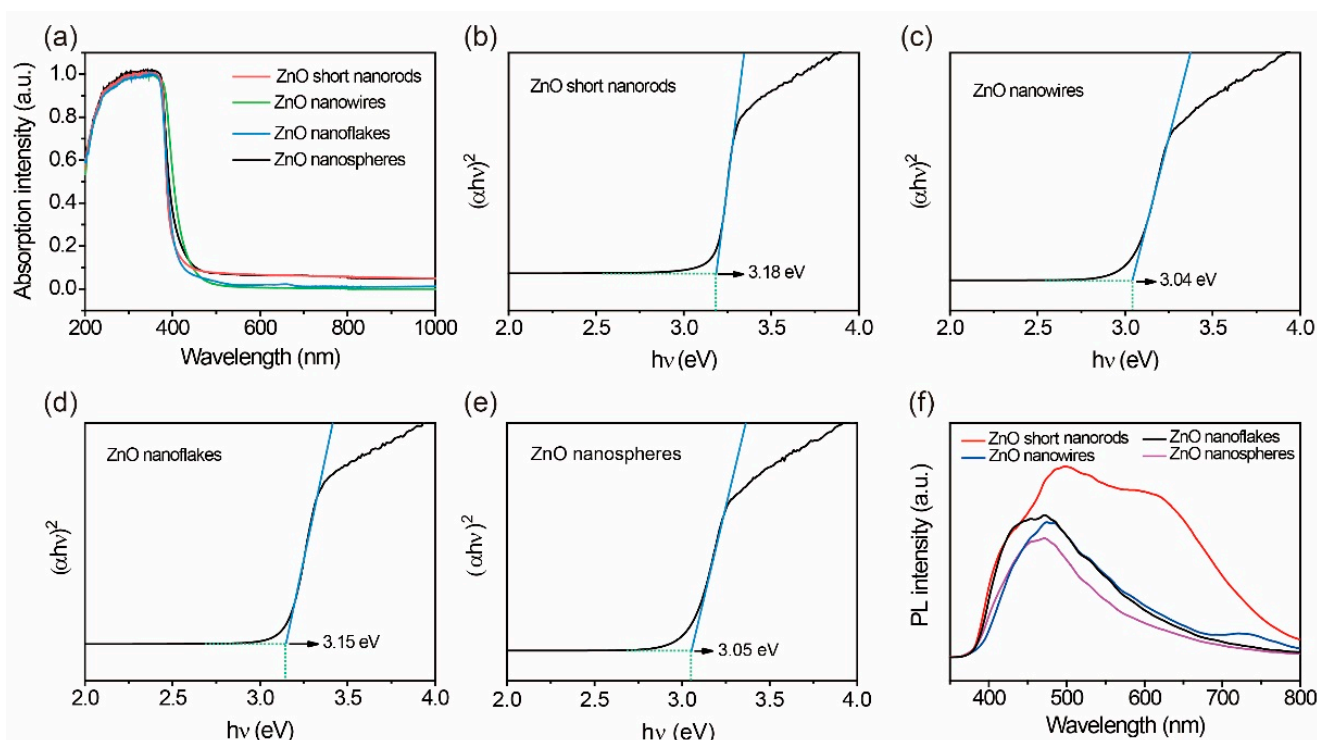


Figure 4. (a) UV-Vis spectra of four ZnO samples. (b–e) Plots of $(\alpha h\nu)^2$ versus photon energy ($h\nu$) for (c) ZnO short nanorods, (d) ZnO nanowires, (e) ZnO nanoflakes, and (f) ZnO nanospheres. (f) PL spectra of four ZnO samples.

BET surface areas of four ZnO samples were measured by testing N_2 adsorption/desorption isotherm at 77 K (Figure 5). The BET surface areas of ZnO samples follow the order: nanoflakes ($8.31 \text{ m}^2 \text{ g}^{-1}$) > nanospheres ($6.47 \text{ m}^2 \text{ g}^{-1}$) > nanowires ($4.32 \text{ m}^2 \text{ g}^{-1}$) > nanorods ($2.86 \text{ m}^2 \text{ g}^{-1}$). ZnO nanorods and nanowires have relatively lower BET surface areas, consistent with their smooth surface and high-crystalline structure as discussed above (Figure 2). The ZnO nanoflakes and nanospheres show higher BET surface areas, which are

attributed to their nanoparticle-assembled structures. Moreover, the adsorption/desorption isotherms for all the samples are quite similar, and no specific porous structures were identified in the nanoflake or nanosphere samples. However, it was noted that the very low BET surface areas of all the samples would not be the determinant for the adsorption property of RhB.

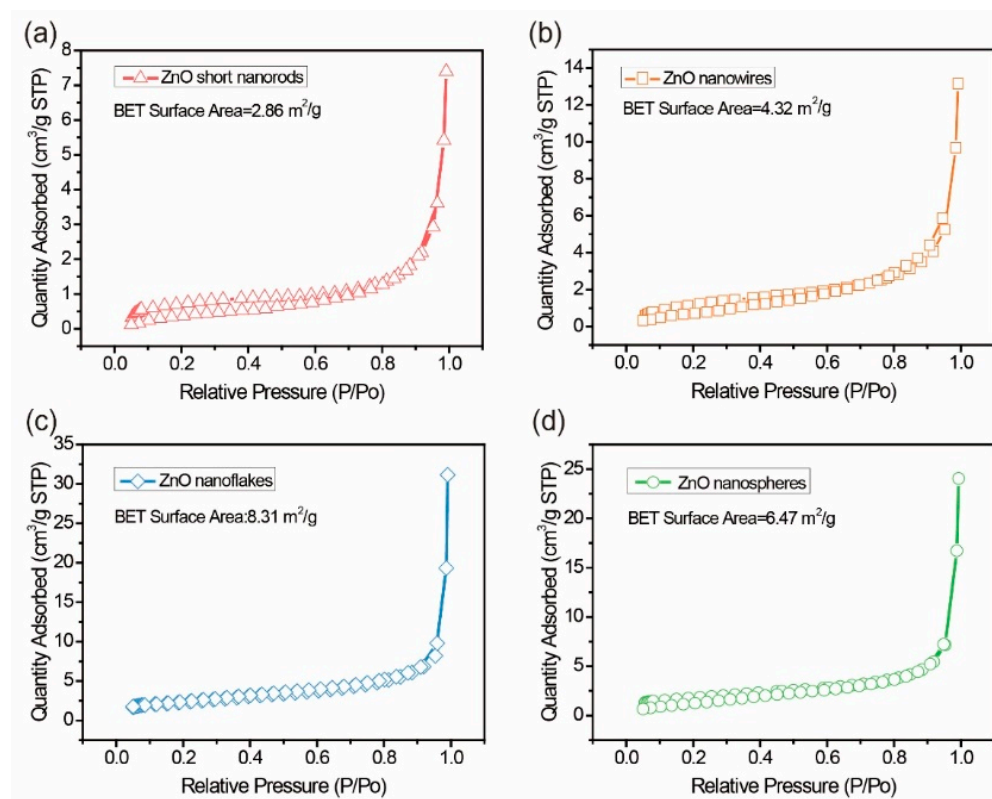


Figure 5. BET curves of (a) ZnO short nanorods, (b) ZnO nanowires, (c) ZnO nanoflakes, and (d) ZnO nanospheres.

To investigate how morphology affected the photocatalytic efficiency and piezoelectric properties of ZnO samples, RhB was used as a model water pollutant to test photocatalytic dye degradation. The piezoelectric effect was verified by comparing photocatalytic performance with or without ultrasound. The photocatalytic degradation curves of ZnO samples are shown in Figure 6. All samples delivered RhB photo-degradation activity. For the ZnO short nanorod sample, RhB could be completely degraded within 30 min with or without ultrasound. The photocatalytic efficiency was slightly improved with ultrasound assistance (see Figure 6a). For the ZnO nanowire sample, the degradation of RhB showed a similar tendency to that for the ZnO short nanorod sample. The RhB was degraded within 20 min and an obviously increased degradation rate was detected with assistance of ultrasound (see Figure 6b). The ZnO nanoflake sample showed comparable photocatalytic activity for degradation of RhB as the above described two samples. However, ultrasound did not affect the degradation rate in this case (see Figure 6c). In comparison, the ZnO nanosphere sample showed relatively poor photocatalytic activity for degradation of RhB, which required 60 min to finish degradation (see Figure 6d). However, under ultrasound, the degradation rate was significantly increased.

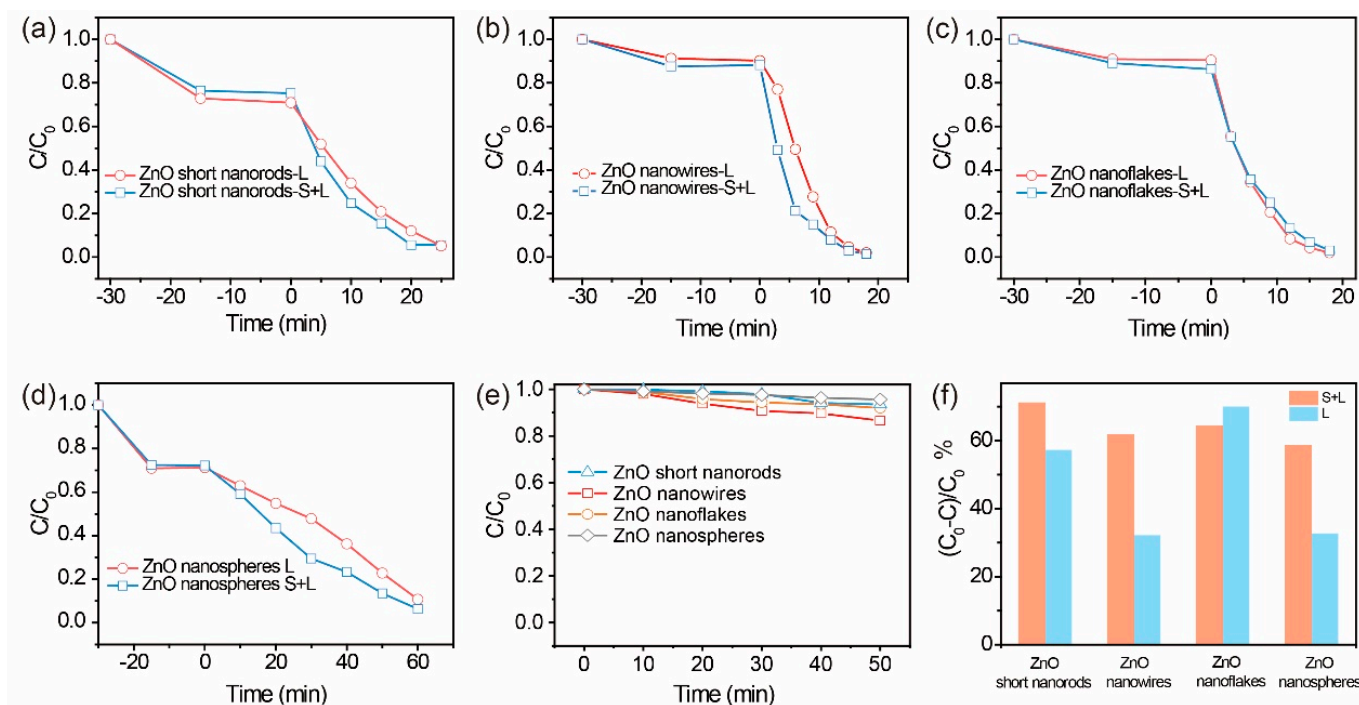


Figure 6. Photocatalytic degradation performance of (a) ZnO short nanorods, (b) ZnO nanowires, (c) ZnO nanoflakes, and (d) ZnO nanospheres. (e) Ultrasonic degradation curves for all the ZnO samples in dark. (f) Degradation enhancement of all samples compared at the points around 70% degradation under S+L condition (L: light illumination only, S+L: light illumination with ultrasound).

As shown in Figure 6e, the ultrasound-derived degradation rates of RhB in dark for the short nanorod, nanoflake, and nanosphere samples are all around 10%, but for the nanowire sample, the degradation rate is around 18%. The enhanced degradation rate is due to the piezoelectric effect of ZnO stimulated by ultrasound. The ZnO nanowire sample possesses both the good crystallinity and easily-stimulated morphology, which endows the best ultrasonic catalytic performance. As shown in Figure 6f, we took the points at 70% degradation under S+L condition for various samples to make comparison. The ZnO short nanorod, nanowire, and nanosphere samples all showed significant improvements under ultrasound. The ZnO short nanorod sample provided a ~15% improvement in photocatalytic efficiency assisted by ultrasound, which is comparable to ultrasound-derived RhB degradation in the dark (~10%, Figure 6e). Thus, the improved photocatalytic property of the ZnO nanorod sample assisted by ultrasound should be the combination of photocatalysis and ultrasonic catalysis. Notably, the improved degradation rate under ultrasound and light for the ZnO nanowire and nanosphere samples were both around 30%, which is much higher than the individual ultrasound-derived RhB degradation. This indicates that ultrasound would enhance the photocatalytic process in this case instead of the addition of the two kinds of catalysis. As discussed in our previous work [53], the enhancement should come from the improved photo-induced charge separation in ZnO driven by piezo-electric field under ultrasonic vibration. Moreover, as discussed in the previous work, the piezoelectric material of BaTiO₃ works as the generator of driving force for charge separation only, while the surface constructed photocatalyst of Ag₂O performs the catalytic process. Different from the heterostructure of BaTiO₃@Ag₂O, the piezoelectric ZnO could combine the functions and work as a self-assisted photocatalysis based on the piezophototronic effect. The ultrasound showed negative effect on the ZnO nanoflake sample, which might be due to that the ultrasonic vibration affected the reaction process via suppressing the adsorption of RhB molecules.

The degradation rate constant (k) was calculated using the equation $\ln(C/C_0) = -kt$. The RhB degradation processes for various ZnO samples follow the pseudo-first-order rate

law [54]. For the ZnO short nanorod sample, the photocatalytic degradation rate constants (k) with and without ultrasound were calculated as 0.107 and 0.078, respectively. The corresponding values for the ZnO nanowire sample were 0.208 and 0.117, respectively, in agreement with the best photocatalytic property and the highest enhancement under ultrasound for the ZnO nanowire sample. However, a negative effect of ultrasound on the photocatalytic process was observed for the ZnO nanoflake sample, the k value decreasing from 0.163 to 0.141 under ultrasound. Notably, for the ZnO nanospheres, the k value doubled from 0.013 to 0.028 by involving the ultrasound during the photocatalytic process. However, the photocatalytic efficiency of the ZnO nanosphere sample was the lowest among all the studied ZnO samples. The above results indicate that different morphologies resulted in different degradation rates. Moreover, the responses to the ultrasound-derived piezoelectric effect in ZnO were different with the morphology change. The ZnO nanowire sample with good crystallinity, more catalytic active surfaces, and excitable deformation, delivered the highest piezophototronic effect and the best photocatalytic performance.

3. Experimental procedures

3.1. Materials

Chemical reagents (analytical grade), such as zinc acetate dihydrate [$\text{Zn}(\text{CH}_3\text{COO})\cdot 2\text{H}_2\text{O}$], zinc nitrate hexahydrate [$\text{Zn}(\text{NO}_3)_2\cdot 6\text{H}_2\text{O}$], sodium hydroxide (NaOH), urea ($\text{CH}_4\text{N}_2\text{O}$), triethanolamine (TEOA), were purchased from Sinopharm Chemical Reagent Co., Ltd. (Shanghai, China) and used without further purification. Distilled water and absolute ethanol were used for preparing solutions and for washing the as-obtained samples.

3.2. ZnO Synthesis

Preparation of ZnO short nanorods: typically, 0.01 mol of $\text{Zn}(\text{CH}_3\text{COO})\cdot 2\text{H}_2\text{O}$ and 0.01 mol of NaOH were dissolved in 100 ml of distilled water separately; the concentration of NaOH solution was 0.1 M. Then, they were mixed and kept at 90 °C for 40 min. After the reaction, the white precipitate was washed by distilled water and ethanol several times and finally dried in a vacuum oven at 60 °C for 12 h.

Preparation of ZnO nanowires: the preparation procedure was the same as that for ZnO short nanorods as described above, except for increasing the dosage of NaOH to 0.1 mol, the concentration of NaOH is 1.0 M.

Preparation of ZnO nanoflakes: 0.2 mol of $\text{Zn}(\text{NO}_3)_2\cdot 6\text{H}_2\text{O}$ and 0.3 mol of urea were dissolved in 40 ml distilled water and stirred for 2 h, then the mixture was put into a Teflon-lined autoclave and maintained at 90 °C for 4 h. After the reaction, the white precipitate was washed and dried.

Preparation of ZnO nanospheres: 1 g of $\text{Zn}(\text{CH}_3\text{COO})\cdot 2\text{H}_2\text{O}$ and 10 ml of TEOA were added into 100 ml distilled water separately, then they were mixed and kept at 90 °C for 1 h. After the reaction, the white precipitate was washed and dried.

All above samples were calcined at 500 °C for 2 h in the furnace after drying to remove the residual TEOA, as well as to improve the crystallinity of samples.

3.3. Characterization

X-ray diffraction (XRD) patterns of all samples were collected on a Bruker D8 Advance powder X-ray diffractometer (Cu K α) at 2θ range between 25°–60° with a 0.02° step interval. Raman spectra were measured using a WiTech alpha 300R confocal Raman Microscopy. Scanning electron microscopy (SEM) images were taken on the Hitachi S-4800 field-emission scanning electron microscope. High-resolution transmission electron microscopy (HRTEM) images were collected using a JEOL JEM 2100 microscope operating at 200 kV. Photoluminescence (PL) spectra were measured by Edinburgh FLS 980. BET data were recorded on the specific surface area and pore size analyzer (Micromeritics ASAP2460). UV-Vis spectra were measured on an Agilent Cary 5000. X-ray photoelectron spectroscopy (XPS) was performed using the Thermo Scientific ESCALAB 250Xi.

3.4. Photocatalytic Property Evaluation

RhB is used as a model organic compound to evaluate the photocatalytic performance of all prepared photocatalysts. The concentration of RhB solution was 30 mg L⁻¹. Typically, 50 mL of RhB solution was mixed with 50 mg of photocatalysts and then stirred in the dark for 30 min to make an adsorption/desorption equilibrium of RhB on the photocatalyst surface. Then, the mixture was illuminated by a simulated sunlight with a 300 W Xenon lamp. Samples were taken every 10 min from the photoreactor and centrifuged and collected for the measurement of UV-Vis spectrophotometry. For ultrasound assisted photocatalysis, the mixture was put into an ultrasonic machine where it was illuminated by the Xenon lamp.

4. Conclusions

In this study, wurtzite ZnO with various morphologies was successfully prepared by a hydrothermal method. RhB was used as a model dye to evaluate the influence of morphology on photocatalytic activity. The ZnO nanowire sample presented a significant improvement in photo-degradation of RhB upon ultrasonic vibration, revealing that the good crystallinity and more exposed active facets benefited the piezoelectric property of ZnO nanowires, thereby improving photo-generated charge separation induced by piezophototronic effect. The self-assisted photocatalysis based on the piezophototronic effect was shown with piezoelectric-photocatalytic materials under ultrasonic treatment. This work also highlights the influence of morphology on piezoelectric field and photocatalytic efficiency, which may result in the new design of photocatalysts for water treatment.

Author Contributions: Conceptualization, X.S. and Y.S.; data curation, X.S. and Y.S.; formal analysis, X.S. and C.C.; funding acquisition, X.Y. and Y.S.; Investigation, Y.S.; Methodology, X.L.Z., H.L. and Y.S.; project administration, H.L.; Resources, X.Z., N.X., X.L.Z. and H.L.; software, X.Z.; Supervision, H.L., X.Y. and Y.S.; validation, H.L.; visualization, X.Z. and N.X.; writing—original draft, X.S.; writing—review & editing, X.S., C.C., X.Y. and Y.S. All authors have read and agreed to the published version of the manuscript.

Funding: This research was funded by National Natural Science Foundation of China, grant number 52072223, 51732007, 52122210, the Shandong Excellent Young Scientists Fund Program (Overseas, 2022HWYQ-005), and the Qilu Young Scholar Funding of Shandong University.

Conflicts of Interest: The authors declare no conflict of interest.

References

1. Bartolomeu, M.; Neves, M.G.P.M.S.; Faustino, M.A.F.; Almeida, A. Wastewater chemical contaminants: Remediation by advanced oxidation processes. *Photochem. Photobiol. Sci.* **2018**, *17*, 1573–1598. [[CrossRef](#)]
2. Miletto, M. Water and Energy Nexus: Findings of the World Water Development Report 2014. In Proceedings of the 11th Kovacs Colloquium on Hydrological Sciences and Water Security: Past, Present and Future, UNESCO Headquarters, Paris, France, 16–17 June 2014.
3. Chiu, Y.-H.; Chang, T.-F.; Chen, C.-Y.; Sone, M.; Hsu, Y.-J. Mechanistic Insights into Photodegradation of Organic Dyes Using Heterostructure Photocatalysts. *Catalysts* **2019**, *9*, 430. [[CrossRef](#)]
4. Chen, S.; Zhang, J.; Zhang, C.; Yue, Q.; Li, Y.; Li, C. Equilibrium and kinetic studies of methyl orange and methyl violet adsorption on activated carbon derived from Phragmites australis. *Desalination* **2010**, *252*, 149–156. [[CrossRef](#)]
5. Gurreri, L.; Tamburini, A.; Cipollina, A.; Micale, G. Electrodialysis Applications in Wastewater Treatment for Environmental Protection and Resources Recovery: A Systematic Review on Progress and Perspectives. *Membranes* **2020**, *10*, 146. [[CrossRef](#)] [[PubMed](#)]
6. Mustafa, R.; Asmatulu, E. Preparation of activated carbon using fruit, paper and clothing wastes for wastewater treatment. *J. Water Process Eng.* **2020**, *35*, 101239. [[CrossRef](#)]
7. Yang, X.; Wang, Z.; Shao, L. Construction of oil-unidirectional membrane for integrated oil collection with lossless transportation and oil-in-water emulsion purification. *J. Membr. Sci.* **2018**, *549*, 67–74. [[CrossRef](#)]
8. Lin, L.; Li, R.-H.; Li, Y.; Xu, J.; Li, X.-Y. Recovery of organic carbon and phosphorus from wastewater by Fe-enhanced primary sedimentation and sludge fermentation. *Process Biochem.* **2016**, *54*, 135–139. [[CrossRef](#)]
9. Routoula, E.; Patwardhan, S.V. Degradation of Anthraquinone Dyes from Effluents: A Review Focusing on Enzymatic Dye Degradation with Industrial Potential. *Environ. Sci. Technol.* **2020**, *54*, 647–664. [[CrossRef](#)]

10. Ma, D.; Yi, H.; Lai, C.; Liu, X.; Huo, X.; An, Z.; Li, L.; Fu, Y.; Li, B.; Zhang, M.; et al. Critical review of advanced oxidation processes in organic wastewater treatment. *Chemosphere* **2021**, *275*, 130104. [[CrossRef](#)] [[PubMed](#)]
11. Serrà, A.; Philippe, L.; Perreault, F.; Garcia-Segura, S. Photocatalytic treatment of natural waters. Reality or hype? The case of cyanotoxins remediation. *Water Res.* **2020**, *188*, 116543. [[CrossRef](#)]
12. Yousefi, S.R.; Alshamsi, H.A.; Amiri, O.; Salavati-Niasari, M. Synthesis, characterization and application of Co/Co₃O₄ nanocomposites as an effective photocatalyst for discoloration of organic dye contaminants in wastewater and antibacterial properties. *J. Mol. Liq.* **2021**, *337*, 116405. [[CrossRef](#)]
13. Orooji, Y.; Tanhaei, B.; Ayati, A.; Tabrizi, S.H.; Alizadeh, M.; Bamoharram, F.F.; Karimi, F.; Salmanpour, S.; Rouhi, J.; Afshar, S.; et al. Heterogeneous UV-Switchable Au nanoparticles decorated tungstophosphoric acid/TiO₂ for efficient photocatalytic degradation process. *Chemosphere* **2021**, *281*, 130795. [[CrossRef](#)] [[PubMed](#)]
14. Cheng, C.; Mao, L.H.; Shi, J.W.; Xue, F.; Zong, S.C.; Zheng, B.T.; Guo, L.J. NiCo₂O₄ Nanosheets as a Novel Oxygen-Evolution-Reaction Cocatalyst in Situ Bonded on the G-C₃N₄ Photocatalyst for Excellent Overall Water Splitting. *J. Mater. Chem. A* **2021**, *9*, 12299–12306. [[CrossRef](#)]
15. Jiang, H.X.; Zhang, L.S.; Liu, H.Y.; Wu, D.S.; Wu, F.Y.; Tian, L.; Liu, L.L.; Zou, J.P.; Luo, S.L.; Chen, B.B. Silver Single Atom in Carbon Nitride Catalyst for Highly Efficient Photocatalytic Hydrogen Evolution. *Angew. Chem.* **2020**, *59*, 23112–23116. [[CrossRef](#)] [[PubMed](#)]
16. Li, D.; Kassymova, M.; Cai, X.; Zang, S.-Q.; Jiang, H.-L. Photocatalytic CO₂ reduction over metal-organic framework-based materials. *Co-ord. Chem. Rev.* **2020**, *412*, 213262. [[CrossRef](#)]
17. Huang, H.Y.; Wang, K.; Guo, T.; Li, J.; Wu, X.Y.; Zhang, G.K. Construction of 2d/2d Bi₂Se₃/G-C₃N₄ Nanocomposite with High Interfacial Charge Separation and Photo-Heat Conversion Efficiency for Selective Photocatalytic CO₂ Reduction. *Appl. Catal. B Environ.* **2020**, *277*, 119232. [[CrossRef](#)]
18. Irshad, M.A.; Nawaz, R.; Rehman, M.Z.U.; Adrees, M.; Rizwan, M.; Ali, S.; Ahmad, S.; Tasleem, S. Synthesis, characterization and advanced sustainable applications of titanium dioxide nanoparticles: A review. *Ecotoxicol. Environ. Saf.* **2021**, *212*, 111978. [[CrossRef](#)]
19. Humayun, M.; Raziq, F.; Khan, A.; Luo, W. Modification Strategies of TiO₂ for Potential Applications in Photocatalysis: A critical Review. *Green Chem. Lett. Rev.* **2018**, *11*, 86–102. [[CrossRef](#)]
20. Guo, C.; Li, L.; Chen, F.; Ning, J.; Zhong, Y.; Hu, Y. One-step phosphorization preparation of gradient-P-doped CdS/CoP hybrid nanorods having multiple channel charge separation for photocatalytic reduction of water. *J. Colloid Interface Sci.* **2021**, *596*, 431–441. [[CrossRef](#)]
21. Huang, Y.X.; Lei, R.; Yuan, J.; Gao, F.; Jiang, C.K.; Feng, W.H.; Zhuang, J.D.; Liu, P. Insight into the Piezo-Photo Coupling Effect of PbTiO₃/CdS Composites for Piezo-Photocatalytic Hydrogen Production. *Appl. Catal. B Environ.* **2021**, *282*, 119586. [[CrossRef](#)]
22. Wang, K.; Xing, Z.P.; Du, M.; Zhang, S.Y.; Li, Z.Z.; Pan, K.; Zhou, W. Hollow MoSe₂@Bi₂S₃/CdS Core-Shell Nanostructure as Dual Z-Scheme Heterojunctions with Enhanced Full Spectrum Photocatalytic-Photothermal Performance. *Appl. Catal. B Environ.* **2021**, *281*, 119482. [[CrossRef](#)]
23. Tan, H.L.; Amal, R.; Ng, Y.H. Alternative strategies in improving the photocatalytic and photoelectrochemical activities of visible light-driven BiVO₄: A review. *J. Mater. Chem. A* **2017**, *5*, 16498–16521. [[CrossRef](#)]
24. Wang, L.Y.; Ding, K.; Xu, R.; Yu, D.; Wang, W.; Gao, P.; Liu, B.J. Fabrication of BiVO₄/BiPO₄/GO Composite Photocatalytic Material for the Visible Light-Driven Degradation. *J. Clean. Prod.* **2020**, *247*, 119108. [[CrossRef](#)]
25. Yu, C.; Li, G.; Kumar, S.; Yang, K.; Jin, R. ChemInform Abstract: Phase Transformation Synthesis of Novel Ag₂O/Ag₂CO₃ Heterostructures with High Visible Light Efficiency in Photocatalytic Degradation of Pollutants. *ChemInform* **2014**, *45*, 892–898. [[CrossRef](#)]
26. Chen, Y.; Zhu, G.; Hojamberdiev, M.; Gao, J.; Zhu, R.; Wang, C.; Wei, X.; Liu, P. Three-dimensional Ag₂O/Bi₅O₇I p-n heterojunction photocatalyst harnessing UV-vis-NIR broad spectrum for photodegradation of organic pollutants. *J. Hazard. Mater.* **2018**, *344*, 42–54. [[CrossRef](#)]
27. Hieu, C.N.; Lien, T.M.; Van, T.T.T.; Juang, R.S. Enhanced Removal of Various Dyes from Aqueous Solutions by UV and Simulated Solar Photocatalysis over TiO₂/ZnO/rGO Composites. *Sep. Purif. Technol.* **2020**, *232*, 115962. [[CrossRef](#)]
28. Kumar, S.G.; Rao, K.S.R.K. Zinc oxide based photocatalysis: Tailoring surface-bulk structure and related interfacial charge carrier dynamics for better environmental applications. *RSC Adv.* **2014**, *5*, 3306–3351. [[CrossRef](#)]
29. Goktas, S.; Goktas, A. A comparative study on recent progress in efficient ZnO based nanocomposite and heterojunction photocatalysts: A review. *J. Alloys Compd.* **2021**, *863*, 158734. [[CrossRef](#)]
30. Pan, L.; Muhammad, T.; Ma, L.; Huang, Z.-F.; Wang, S.; Wang, L.; Zou, J.-J.; Zhang, X. MOF-derived C-doped ZnO prepared via a two-step calcination for efficient photocatalysis. *Appl. Catal. B Environ.* **2016**, *189*, 181–191. [[CrossRef](#)]
31. Trandafilovic, V.L.; Jovanovic, D.J.; Zhang, X.; Ptasinska, S.; Dramicanin, M.D. Enhanced Photocatalytic Degradation of Methylene Blue and Methyl Orange by ZnO:Eu Nanoparticles. *Appl. Catal. B Environ.* **2017**, *203*, 740–752. [[CrossRef](#)]
32. Ardekani, R.S.; Aghdam, A.S.R.; Nazari, M.; Bayat, A.; Saievar-Iranizad, E.; Liavali, M.N. Synthesis and Characterization of Photocatalytically Active Crumpled-Shape Nanocomposites of Nitrogen and Sulfur Co-Doped ZnO-CeO₂. *Sol. Energy Mater. Sol. Cells* **2019**, *203*, 110195. [[CrossRef](#)]

33. Bharathi, P.; Harish, S.; Archana, J.; Navaneethan, M.; Ponnusamy, S.; Muthamizhchelvan, C.; Shimomura, M.; Hayakawa, Y. Enhanced charge transfer and separation of hierarchical CuO/ZnO composites: The synergistic effect of photocatalysis for the mineralization of organic pollutant in water. *Appl. Surf. Sci.* **2019**, *484*, 884–891. [[CrossRef](#)]
34. Aliaga, J.; Cifuentes, N.; González, G.; Sotomayor-Torres, C.; Benavente, E. Enhancement Photocatalytic Activity of the Hetero-junction of Two-Dimensional Hybrid Semiconductors ZnO/V₂O₅. *Catalysts* **2018**, *8*, 374. [[CrossRef](#)]
35. Wang, Z.L.; Wu, W.; Falconi, C. Piezotronics and piezo-phototronics with third-generation semiconductors. *MRS Bull.* **2018**, *43*, 922–927. [[CrossRef](#)]
36. Yang, Q.; Wang, W.; Xu, S.; Wang, Z.L. Enhancing Light Emission of ZnO Microwire-Based Diodes by Piezo-Phototronic Effect. *Nano Lett.* **2011**, *11*, 4012–4017. [[CrossRef](#)]
37. Xue, X.; Zang, W.; Deng, P.; Wang, Q.; Xing, L.; Zhang, Y.; Wang, Z.L. Piezo-potential enhanced photocatalytic degradation of organic dye using ZnO nanowires. *Nano Energy* **2015**, *13*, 414–422. [[CrossRef](#)]
38. Bai, Y.; Zhao, J.; Lv, Z.; Lu, K. Enhanced piezo-phototronic effect of ZnO nanorod arrays for harvesting low mechanical energy. *Ceram. Int.* **2019**, *45*, 15065–15072. [[CrossRef](#)]
39. Wu, W.; Yin, X.; Dai, B.; Kou, J.; Ni, Y.; Lu, C. Water flow driven piezo-photocatalytic flexible films: Bi-piezoelectric integration of ZnO nanorods and PVDF. *Appl. Surf. Sci.* **2020**, *517*, 146119. [[CrossRef](#)]
40. Hong, K.-S.; Xu, H.; Konishi, H.; Li, X. Direct Water Splitting Through Vibrating Piezoelectric Microfibers in Water. *J. Phys. Chem. Lett.* **2010**, *1*, 997–1002. [[CrossRef](#)]
41. Wu, J.M.; Sun, Y.-G.; Chang, W.-E.; Lee, J.-T. Piezoelectricity induced water splitting and formation of hydroxyl radical from active edge sites of MoS₂ nanoflowers. *Nano Energy* **2018**, *46*, 372–382. [[CrossRef](#)]
42. Raoufi, D. Synthesis and microstructural properties of ZnO nanoparticles prepared by precipitation method. *Renew. Energy* **2013**, *50*, 932–937. [[CrossRef](#)]
43. Vorokh, A. Scherrer formula: Estimation of error in determining small nanoparticle size. *Nanosyst. Phys. Chem. Math.* **2018**. [[CrossRef](#)]
44. Montenegro, D.N.; Hortelano, V.; Martínez, O.; Martínez-Tomas, M.C.; Sallet, V.; Muñoz-Sanjose, V.; Jiménez, J. Non-radiative recombination centres in catalyst-free ZnO nanorods grown by atmospheric-metal organic chemical vapour deposition. *J. Phys. D Appl. Phys.* **2013**, *46*. [[CrossRef](#)]
45. Walter, C.; Barg, S.; Ni, N.; Maher, R.C.; García-Tuñón, E.; Ismail, M.M.Z.; Babot, F.; Saiz, E. A novel approach for the fabrication of carbon nanofibre/ceramic porous structures. *J. Eur. Ceram. Soc.* **2013**, *33*, 2365–2374. [[CrossRef](#)]
46. Su, X.; Wang, Z.; Huang, Y.; Miao, Z.; Wang, S.; Wang, J.; Zhang, X.L.; Sun, X.; Liu, H.; Sang, Y. Triethanolamine interface modification of crystallized ZnO nanospheres enabling fast photocatalytic hazard-free treatment of Cr(vi) ions. *Nanotechnol. Rev.* **2021**, *10*, 847–856. [[CrossRef](#)]
47. Rambabu, K.; Bharath, G.; Banat, F.; Show, P.L. Green synthesis of zinc oxide nanoparticles using Phoenix dactylifera waste as bioreductant for effective dye degradation and antibacterial performance in wastewater treatment. *J. Hazard. Mater.* **2020**, *402*, 123560. [[CrossRef](#)]
48. Cao, C.; Xie, X.; Zeng, Y.; Shi, S.; Wang, G.; Yang, L.; Wang, C.-Z.; Lin, S. Highly efficient and stable p-type ZnO nanowires with piezotronic effect for photoelectrochemical water splitting. *Nano Energy* **2019**, *61*, 550–558. [[CrossRef](#)]
49. Yu, S.; Zhang, H.; Li, Z. Effects of pH on High-Performance ZnO Resistive Humidity Sensors Using One-Step Synthesis. *Sensors* **2019**, *19*, 5267. [[CrossRef](#)]
50. Zhang, Q.; Gu, H.; Wang, X.; Li, L.; Zhang, J.; Zhang, H.; Li, Y.-F.; Dai, W.-L. Robust hollow tubular ZnIn₂S₄ modified with embedded metal-organic-framework-layers: Extraordinarily high photocatalytic hydrogen evolution activity under simulated and real sunlight irradiation. *Appl. Catal. B Environ.* **2021**, *298*, 120632. [[CrossRef](#)]
51. Li, W.; Wang, G.; Chen, C.; Liao, J.; Li, Z. Enhanced Visible Light Photocatalytic Activity of ZnO Nanowires Doped with Mn²⁺ and Co²⁺ Ions. *Nanomaterials* **2017**, *7*, 20. [[CrossRef](#)]
52. Li, Q.; Fu, S.; Song, C.; Wang, G.; Zeng, F.; Pan, F. Sputtering power dependence of structure and photoluminescence of ZnO on 6H-SiC. *J. Mater. Sci. Mater. Electron.* **2017**, *28*, 17881–17888. [[CrossRef](#)]
53. Li, H.; Sang, Y.; Chang, S.; Huang, X.; Zhang, Y.; Yang, R.; Jiang, H.; Liu, H.; Wang, Z.L. Enhanced Ferroelectric-Nanocrystal-Based Hybrid Photocatalysis by Ultrasonic-Wave-Generated Piezophototronic Effect. *Nano Lett.* **2015**, *15*, 2372–2379. [[CrossRef](#)] [[PubMed](#)]
54. Zhao, C.; Liang, Y.; Li, W.; Tian, Y.; Chen, X.; Yin, D.; Zhang, Q. BiOBr/BiOCl/carbon quantum dot microspheres with superior visible light-driven photocatalysis. *RSC Adv.* **2017**, *7*, 52614–52620. [[CrossRef](#)]